Contents lists available at ScienceDirect

Transactions of Nonferrous Metals Society of China

36(2026) 659−676

www.tnmsc.cn

Characteristics of gas−liquid flow in double-side-blown systems computed by CFD

Wei WANG [a,b], Hong-liang ZHAO [a,b,*], Feng-qin LIU [a,b], Hong Yong SOHN [c]

[a] State Key Laboratory of Advanced Metallurgy, University of Science and Technology Beijing, Beijing 100083, China;
[b] School of Metallurgical and Ecological Engineering, University of Science and Technology Beijing, Beijing 100083, China;
[c] Department of Materials Science and Engineering, The University of Utah, Salt Lake City, Utah 84112, USA

Abstract: A CFD-based numerical model was employed to quantitatively analyze the flow characteristics of double-side-blown gas−liquid flow. Key parameters were extracted, and Spearman correlation analysis was used to quantify the relationships among bubble behavior, circulating flow, and liquid oscillations. The results show that periodic bubble behavior under steady injection drives the circulating flow of the liquid on both sides. The asynchronism of bubble behavior on both sides results in the alternation of circulating intensity, which significantly enhances gas−liquid mixing efficiency at certain liquid levels of 200 and 220 mm. Flow patterns of the double-side-blown process are classified into weak circulation, strong−weak alternating circulation, and strong circulation modes based on the influence of circulating flows on the penetration depth. The penetration depth in the strong−weak alternating circulation mode is generally greater than that in the single-side-blown process. The imbalance of circulating intensities on both sides primarily leads to the stable fluctuation in the injecting direction, which reveals the appearance of periodic oscillations in the molten bath. The effect of control parameters such as liquid level and gas flow rate on the liquid oscillations were discussed.

Keywords: numerical simulation; side-blown furnace; flow characteristics; bubble behavior; penetration depth; Spearman correlation analysis

1 Introduction

In pyrometallurgy, the oxygen-enriched side-blown smelting technology has received much attention due to its advantages of strong adaptability to raw materials, high smelting intensity, effective impurity removal capacity, high economic benefits, and low environmental effects [1−3]. This technology has been widely applied in the extraction and smelting of copper [4], lead [5,6], and secondary resources [7], as well as in the collaborative treatment of solid wastes [8]. To optimize smelting parameters and better understand the characteristics and interactions of multiphase flow in side-blown furnaces, researchers usually employ numerical simulations based on computational fluid dynamics (CFD) and cold-model experiments based on similarity principles [9−14]. The present research mainly focuses on gas penetration depth [15], jet trajectories [16], flow patterns [17], mixing behavior [18], and emulsification phenomena [19].

The penetration depth (PD) of submerged side-blown gas is defined as the farthest horizontal distance from the nozzle outlet to the gas−liquid boundary [15,20]. HOEFELE and BRIMACOMBE [20] recorded the PD of an argon oxygen decarburization (AOD)-converter under various gas−liquid systems, tuyere sizes, and gas flow rates, and derived an empirical correlation for PD. MA et al [21]

Corresponding author: *Hong-liang ZHAO, Tel: +86-18618336024, E-mail: zhaohl@ustb.edu.cn
https://doi.org/10.1016/S1003-6326(25)66989-5
Received 8 August 2024; accepted 19 May 2025

established a dimensionless model for PD, and determined the PD from images captured during cold-model experiments by MATLAB. ZHU et al [15] also determined the PD from time-averaged images by MATLAB to develop a correlation between PD and nozzle tilt angle. Through water-model experiments, WANG et al [22] discovered that the relationship between the PD and gas flow rate approximates a parabolic curve, and the PD is relatively unaffected by changes in liquid level and nozzle height.

The PD is one of the critical characteristics of gas injection in the submerged side-blown gas−liquid flow process. It is easily captured by a high-speed camera in cold experiments and is commonly used for comparison and validation against the simulation results [23]. Previous studies indicated that under constant steady flow, the gas−liquid flow pattern transitions from bubbly flow to steady jet flow as the PD or modified Froude number (*Fr*) increases [15,20,24]. Further, XIAO et al [25,26] conducted water-model experiments and numerical simulations on the oxygen-enriched side-blown copper smelting furnace (OBSF), identifying the predominant flow pattern as bubble flow. They categorized the lifecycle of individual bubbles into three stages: bubble formation, detachment, and floating-breakup. HU et al [27] divided the bubble rise trajectory into four zones: momentum, transition, jetting, and surface zone.

Other studies have focused on the optimization and design of operational parameters of the OBSF based on CFD. XIAO et al [26] and WAN et al [28] proposed adjusting nozzle arrangement and operating parameters to improve the circulating flow. BIAN et al [29] used an orthogonal experimental design to investigate the effects of nozzle arrangement, nozzle immersion depth, nozzle tilt angle, and nozzle diameter on the flow field. In contrast to constant gas flow, SU et al [30] used variable gas flow rates. They found that sinusoidal and rectangular waveform injection velocities effectively mitigated dead zones.

Research on the characteristics of double-side-blown gas-liquid flow is relatively scarce. Among related studies, ZHOU et al [31] categorized the single-side-blown flow patterns into three types: bubbly flow, slug flow, and intermittent flow. XIAO et al [25,26] divided the bubble flow field in the double-side-blown process into five regions, namely high-speed injection, strong-loop, weak-loop, gas overflow, and separation and settlement. WANG et al [32] observed macro-instability phenomenon with periodic oscillations of the liquid under specific conditions in the double-side-blown process. This phenomenon could be mitigated or eliminated by adjusting operational parameters, although the exact cause remains unclear. In studies of other similar multiphase reactors, SHUI et al [33] observed different types of surface waves in the lab-scale model of a bottom-blown copper bath smelting furnace and investigated longitudinal waves in another study [34]. OBISO et al [35] adopted numerical quantification methods to reveal that the rotational sloshing waves in a top-submerged-lance cylindrical metal bath were induced by the gas flow. TERNSTEDT et al [36] identified three different flow patterns in an AOD converter with a single-side-blown injection. FABRITIUS et al [37] arrived at similar conclusions, and they also studied the oscillation of the molten bath, attributing the bath oscillation to the symmetry of the plume on the vertical axis of the vessel caused by deep penetration of the gas jets. Investigation of the interaction between the gas injection and flow circulation in the double-side-blown process is crucial to explaining these phenomena, yet current research in this area remains insufficient, especially in terms of quantitative analysis.

To fill this gap, our work aims to explore a method to quantitatively reveal the interaction of bubble behavior, circulating flow, and liquid oscillation in the double-side-blown gas−liquid two-phase flows. Transient simulation of a lab-scale OBSF model was performed to extract the key features of gas−liquid two-phase flows. The reliability of the numerical model was validated by a cold-model experiment. The Spearman correlation analysis was introduced to quantitively investigate the correlations among various key parameters. The flow patterns in the double-side-blown process were also discussed.

2 Model construction

In the numerical simulation of bath smelting furnaces, the volume of fluid (VOF) multiphase flow model coupled with the realizable k−ε turbulence model is commonly used to describe the gas−slag−matte multiphase system. Therefore, this work also

adopted the same numerical model, which has been applied and validated in similar research [23,26,27]. All numerical cases were implemented in the commercial software ANSYS Fluent. The geometric model was simplified as follows: (1) The model ignored the presence of the top feed inlet for raw materials as well as the matte and slag tapping holes; (2) The initial flow field was static and the chemical reactions were not included; (3) Both the gas and liquid phases were treated as incompressible fluids with continuous and stable properties.

2.1 Volume of fluid method

In the VOF multiphase flow model, the liquid phase was selected as the primary phase, and the gas phase was set as the secondary phase. The volume fractions of two gas−liquid phases were calculated by following continuity equations:

$$\frac{\partial}{\partial t}(\alpha_g\rho_g)+\nabla(\alpha_g\rho_g\vec{v})=0 \tag{1}$$

$$\alpha_g+\alpha_l=1 \tag{2}$$

where α_g and α_l are the volume fraction of the gas phase and liquid phase, respectively, ρ_g is the density of the gas phase, and $\vec{v}$ is the velocity of the fluid. All phases share the same fluid velocity $\vec{v}$, which is calculated by a momentum equation expressed by

$$\frac{\partial}{\partial t}(\rho\vec{v})+\nabla(\rho\vec{v}\vec{v})= -\nabla p+\nabla[\mu(\nabla\vec{v}+\nabla\vec{v}^{\mathrm{T}})]+\rho\vec{g}+f_{st} \tag{3}$$

where ρ is the volume-averaged density, p is the pressure, μ is the effective viscosity, $\vec{g}$ is the acceleration of gravity, and f_{st} is the interfacial tension between any two phases. The volume-averaged density and effective viscosity are calculated by

$$\rho=\alpha_g\rho_g+\alpha_l\rho_l \tag{4}$$

$$\mu=\alpha_g\mu_g+\alpha_l\mu_l \tag{5}$$

where μ_q is the viscosity of the q phase. The surface tension f_{st} is calculated by the continuum surface force model. Since only gas and liquid phases are included, the calculus of f_{st} is simplified as

$$f_{st}=\sigma\frac{\rho\kappa\nabla\alpha}{0.5(\rho_g+\rho_l)} \tag{6}$$

where κ is the surface curvature and is computed from local gradients in the surface normal to the interface, α is the volume fraction of phase, and σ is the tension. Related formulas are as follows:

$$\kappa=\nabla\cdot\hat{n} \tag{7}$$

$$\hat{n}=n/|n| \tag{8}$$

$$n=\nabla\alpha_g \tag{9}$$

where $\hat{n}$ represents unit normal vectors, and n is the surface normal vector, characterized by the gradient of gas volume fraction α_g.

2.2 Realizable k−ε turbulence model

The realizable k−ε turbulence model was employed to simulate the turbulent flow. This turbulence model accurately simulates the transport and dissipation of turbulent energy by accounting for the nonlinear relationship between dissipation rate (ε) and turbulent kinetic energy (k). The modeled transport equations for k and ε in the realizable k−ε model are

$$\frac{\partial}{\partial t}(\rho k)+\nabla(\rho\vec{v}k)=\nabla\left[\left(\mu+\frac{\mu_t}{\sigma_k}\right)\nabla k\right]+G_k-\rho\varepsilon \tag{10}$$

and

$$\frac{\partial}{\partial t}(\rho\varepsilon)+\nabla(\rho\vec{v}\varepsilon)=\nabla\left[\left(\mu+\frac{\mu_t}{\sigma_\varepsilon}\right)\nabla\varepsilon\right]+\rho C_1S\varepsilon-\rho C_2\frac{\varepsilon^2}{k+\sqrt{\upsilon\varepsilon}} \tag{11}$$

with

$$C_1=\max\left[0.43,\frac{\eta}{\eta+5}\right]$$

$$\eta=S\frac{k}{\varepsilon}$$

$$S=\sqrt{2S_{ij}S_{ij}}$$

where υ is the kinematic viscosity, μ_t is the turbulent viscosity, and G_k represents the generation of turbulence kinetic energy due to the mean velocity gradients. They can be calculated by following equations:

$$\mu_t=\rho\frac{C_\mu k^2}{\varepsilon},\ G_k=\mu_tS^2 \tag{12}$$

where S is the modulus of the mean rate-of-strain tensor, C_μ is a constant, and σ_k and σ_ε are the turbulence Prandtl numbers for k and ε. Compared to two other turbulence models in the k−ε series, C_μ in the expression of the eddy viscosity coefficient of the

realizable k−ε turbulence model is no longer an empirical constant but a function of average strain, rotation rate, angular velocity of system rotation, and the turbulent fields. The model constants are C_2=1.9, σ_k=1.0, σ_ε=1.2.

2.3 Geometry model and mesh configuration

The original OBSF has a repeated configuration of nozzles arrangement. Thus, the injecting area with two symmetrically placed nozzles was selected and scaled down to a laboratory-sized reactor at a ratio of 10:1. As shown in Fig. 1, the main region of the gas−liquid two-phase flow was chosen as the computational domain, which has dimensions of 400 mm × 60 mm × 640 mm. The geometric parameters are listed in Table 1.

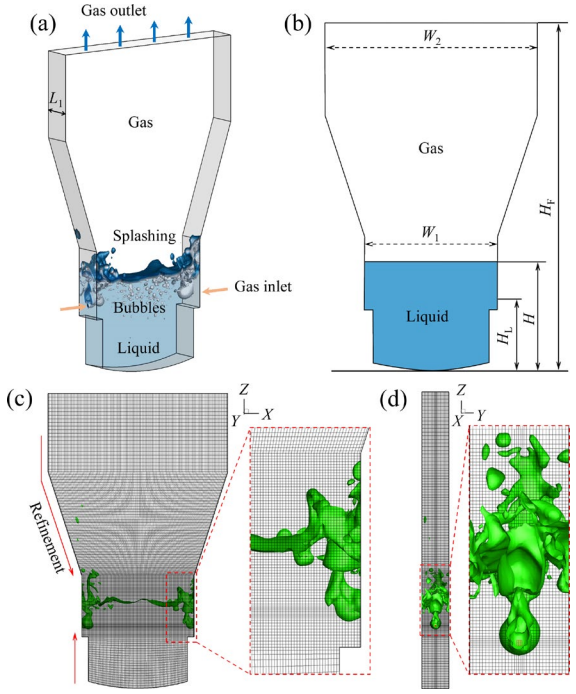

Fig. 1 Schematic diagrams of geometric and mesh models: (a) Computational domain; (b) Gas−liquid distribution at initialization; (c) Front view of mesh model; (d) Mesh structure around nozzle

The mesh model of the fluid domain was constructed with hexahedral meshes. As depicted in Fig. 1, the number of meshes near the nozzles were appropriately refined with smooth transitions to ensure a high resolution of geometric reconstruction at the gas−liquid interfaces, while it was reduced near the outlet to enhance computational efficiency. The circular nozzles in the original furnace with a diameter of 3.8 mm were modeled as square inlets with a side length of 3.4 mm. The minimum orthogonal quality of the mesh model was 0.95 (close to a cube).

2.4 Numerical setting

The physical properties in this work are listed in Table 2, and the solver configurations of numerical model are presented in Table 3.

The nozzles of the numerical model were set as a boundary condition for gas velocity with a range of 29−61 m/s, corresponding to the Fr with a range of 20.58−122.55. The Fr and the inlet turbulence intensity (I) were calculated by

$$Fr=\frac{\rho_g v^2}{(\rho_l-\rho_g)gd} \tag{13}$$

$$I=0.16Re^{-1/8},\ Re=\frac{\rho v D_H}{\mu} \tag{14}$$

where v is inlet velocity, d is the inlet diameter, Re is the Reynolds number, and D_H is the hydraulic diameter. The top outlet was set as the pressure outlet with the gauge pressure of 0 Pa, the backflow turbulence intensity of 5%, and the backflow turbulence viscosity ratio of 0.1225. The residual of each control variable was set as 1.0×10^{-3}.

It is meaningful to study the time-averaged flow field in the double-side-blown process due to the periodic movement. The time-averaged value of variable is computed in each cell of the domain by

Table 1 Geometrical parameters

Model length, L_1/mm	Model width, W_2/mm	Model height, H_F/mm	Nozzle diameter, D/mm	Nozzle height, H_L/mm	Bath width, W_1/mm	Liquid level at initialization, H/mm
60	400	640	3.8	112.3	250	160−240

Table 2 Operating parameters

Gas density, ρ_g/(kg·m^{-3})	Liquid density, ρ_l/(kg·m^{-3})	Gas viscosity, μ_g/(Pa·s)	Liquid viscosity, μ_l/(Pa·s)	Gas−liquid interfacial tension, σ_{gl}/(N·m^{-1})	Inlet velocity, v/(m·s^{-1})	Liquid level, H/mm
1.225	1000	1.8×10^{-5}	0.001	0.072	19-61	160−240

Table 3 Numerical setup

Item	Model/Scheme
Multiphase	VOF-implicit, interfacial modeling type: sharp (interfacial anti-diffusion), continuum surface force model for σ_{gl}
Viscous	Realizable k−ε turbulence model, near-wall treatment: standard wall functions
Solution methods	Pressure-velocity coupling SIMPLE scheme, pressure: PRESTO!, momentum: second order upwind, turbulence: first order upwind
Discretization	Time step size: 1×10^{-4} (Courant number < 5)

$$\overline{\phi}=\frac{1}{T}\int_0^T\phi_t\mathrm{d}t \tag{15}$$

where ϕ is the flow variable, $\overline{\phi}$ is the time-average value of ϕ during the total time T, and ϕ_t is the transient value of ϕ at one time step. All numerical quantities were computed to a total of 25 s. The initial transient development of the flow was excluded by removing the first 5 s of the simulation from the statistical analysis of real physical time.

3 Model validation

3.1 Grid independence

Four sets of mesh models with cell numbers of 368750, 653664, 986622 and 1315820 were used in the grid independence determination, and the results are presented in Fig. 2. It is evident from Fig. 2(a) that after 5 s, the case of 368750 cells exhibited significant changes and overall low velocity, while the other three cases fluctuated within a relatively narrow range. In Fig. 2(b), the other three cases demonstrated a better description of gas−liquid distribution, indicated by the difference in the area circles by the dashed line in 'Mesh 1' from the other cases. Therefore, considering the computational time and solution accuracy, the mesh size of 653664 cells was selected for this work.

3.2 Water-model experiment

A cold-model experiment was conducted to validate the accuracy of the numerical results with the configuration shown in Fig. 3(a). The experimental equipment and procedures used in this work were detailed in a previously published work of our team [25]. Python was used for programming and processing the images captured by the high-speed camera. The steps of image processing are shown in Fig. 3(b). A detailed description of the image-processing procedures can be found by ZHU et al [15]. The comparison results between the experiment and simulation are shown in Figs. 3(c)−(e). General agreement between the experimental and numerical results validated the suitability of the VOF multiphase flow model coupled with the realizable k−ε turbulence model in describing gas−liquid two-phase flow. Further, the dimensionless PD (the ratio of PD to nozzle diameter, L/D) showed a linear relationship with inlet velocity (v), which is consistent with the results of FABRITIUS et al [36].

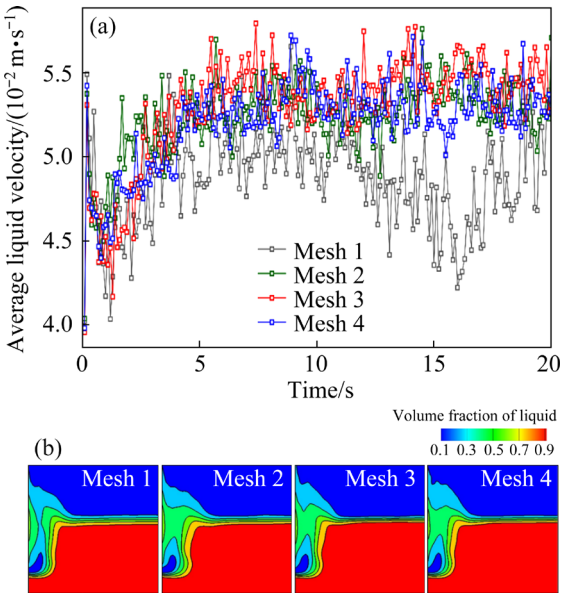

Fig. 2 Results of grid independence test: (a) Average liquid velocity over time; (b) Time-averaged volume fraction of liquid at Y=0.0 m cross-section (Mesh 1: 368750; Mesh 2: 653664; Mesh 3: 986622; Mesh 4: 1315820)

4 Result and discussion

4.1 Characteristic parameters

This section focuses on describing the critical regions extracted from the transient and mean flow fields, providing the information for quantitative characterization of the interaction between bubble behavior and the circulating flow.

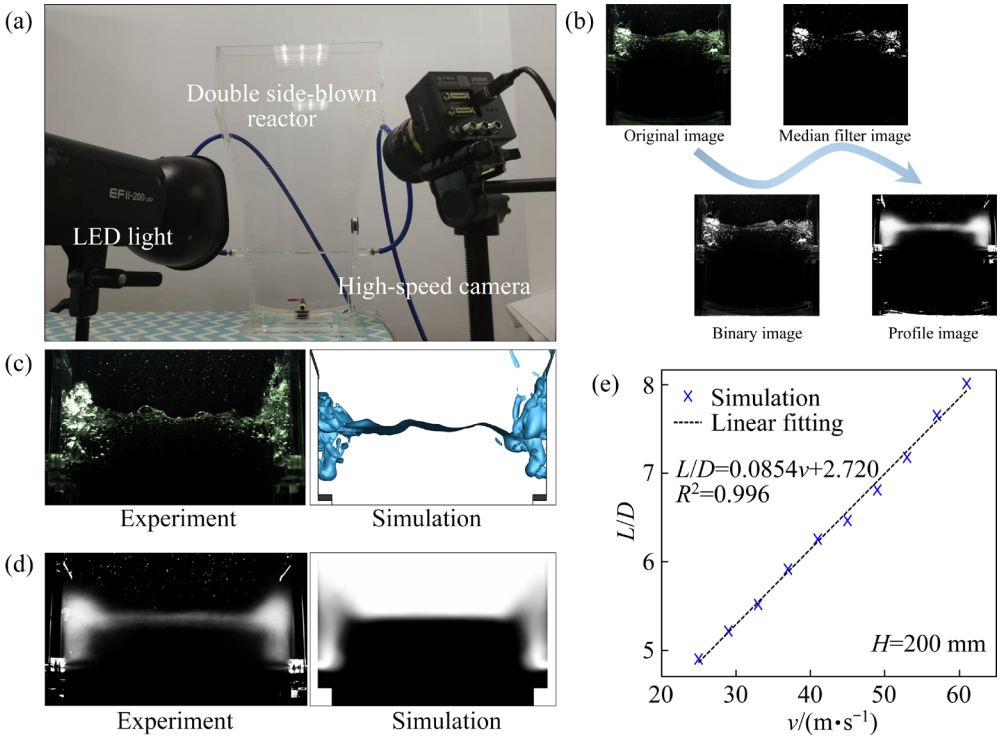

Fig. 3 Cold-model experiments and model validation: **(**a) Schematic diagram of experimental facility; (b) Steps of image processing; (c) Transient flow field; (d) Time-averaged flow field; (e) Dimensionless penetration depth in single-side-blown processing

4.1.1 Analysis of flow field

The flow field significantly affects the gas−liquid mixing efficiency, chemical reaction rate, and the stable operation of the furnace. It was observed that the flow field generally exhibits periodic changes under symmetric geometry and boundary conditions in this work. This phenomenon was also obtained in similar studies [25,34]. The visualization of the circulating flow and the evolution of the bubbles is presented in Fig. 4. The plane of velocity contour is located at Y=0.03 m (through the center of the gas inlets) and the gas fraction (α_g) at the white iso-surface is 0.5. The velocity distribution is filtered, blanking the regions where α_g>0.5. At t=7.94 s, the floating bubbles on the left side push the surrounding liquid continuously toward the center, concurrently driving the liquid below it upward, thereby forming a circulating flow in the left region of the reactor. A similar process occurs on the right side. The liquids from both circulating zones converge at the upper part of the reactor and then move downward, facilitating the circulating flow of the lower liquid. The growth of the bubbles on the right side impedes this circulation, resulting in noticeably smaller and slower circulation compared to the left side. From 7.94 to 7.98 s, the left region experiences the ascent of the bubbles until new bubbles form and grow, whereas on the right side, the bubbles form and ascend. The floatation of bubbles causes the liquid in their original position and below to flow upward, forming a liquid region with a velocity exceeding 0.04 m/s, designated as the "upward flow zone" in this work. It is evident that as the driving force of floating bubbles on the surrounding liquid phase increases, the volume of the upward flow zone should also increase accordingly.

As illustrated in Fig. 4(b), the gas injected into the liquid attempts to maintain a spherical shape to withstand the drag force induced by the liquid [38]. This causes the growing bubble to continuously displace the surrounding liquid, hindering the upward movement of the liquid below the bubble and thereby reducing the volume of the upward flow zone. When the bubble reaches a certain size, it detaches and begins to rise, while the liquid below it rapidly occupies the original position of the bubble, resulting in an expansion of the upward flow zone. This process indicates that the upward flow zone exhibits high sensitivity to the bubble behavior.

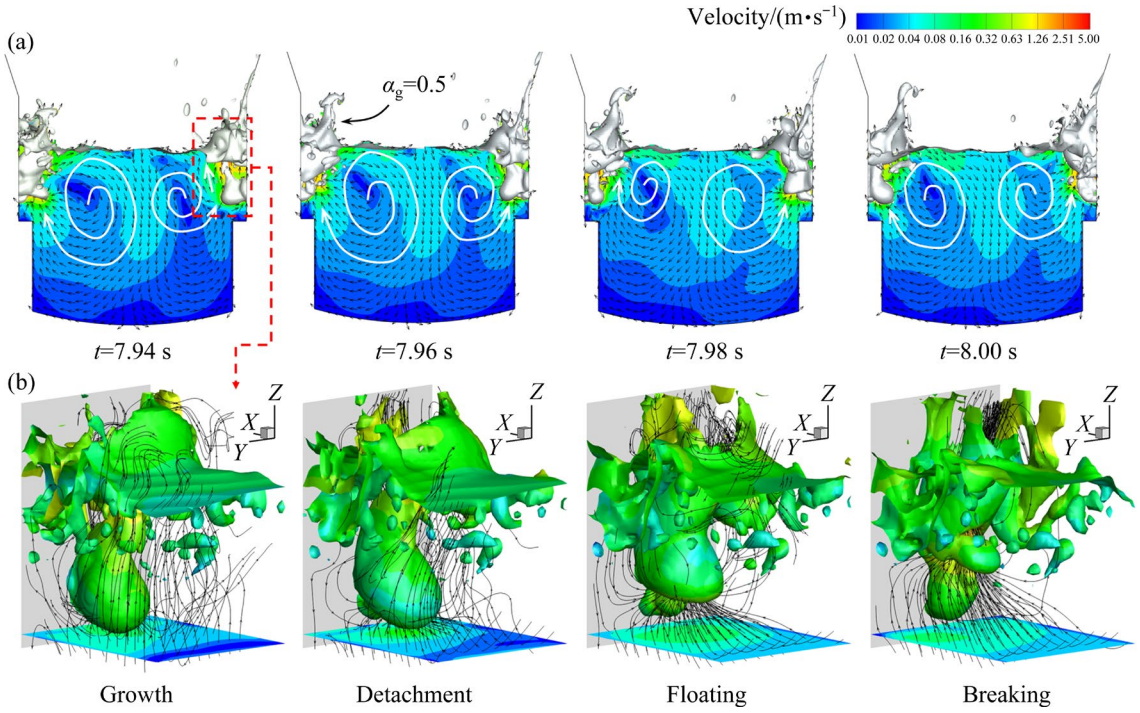

Fig. 4 Circulating flow and bubble behaviors in transient flow field (v=37 m/s, H=200 mm): (a) Evolution of circulating flow over time; (b) Bubble behavior on right side of (a) and streamlines around it

Additionally, the liquid phase within this zone primarily interacts with the injected gas during its ascent, and its volume substantially reflects the intensity of gas stirring and the efficiency of the gas−liquid reaction.

The time-averaged flow field of the double-side-blown gas−liquid process is presented in Fig. 5. Based on the flow characteristics, the flow field can be divided into the injecting zone, the circulating zone, and the settling zone. The circulating zone includes two symmetric small circulation zones on both sides, each containing an upward flow zone formed by the floating bubbles. Figures 5(b) and (c) reveal that the injecting zone is characterized by high turbulence, promoting effective gas−liquid mixing and rapid mass transfer and heat exchange. In contrast, the central part of the flow field exhibits low turbulence, contributing to the stable formation of circulation. It is observed that the upward flow zones within the circulating zone connect the high- and low-turbulence areas, significantly influencing the interfacial mass and heat transfer.

4.1.2 Feature extraction

A parallel user defined function (UDF) was written and compiled to compute and record the characteristic parameters extracted from the numerical model at every time step. The definitions and importance of these parameters were quantified as follows.

The center of mass (CoM) of the liquid phase represents the average position of the liquid phase and is important for understanding the distribution and stability of the liquid phase. The CoM in three dimensions was calculated by the following formulas:

$$\text{CoM-}X=\frac{\sum_{i=1}^{n}V_i(1-\alpha_{\text{g},i})X_i}{\sum_{i=1}^{n}V_i(1-\alpha_{\text{g},i})} \tag{16}$$

$$\text{CoM-}Y=\frac{\sum_{i=1}^{n}V_i(1-\alpha_{\text{g},i})Y_i}{\sum_{i=1}^{n}V_i(1-\alpha_{\text{g},i})} \tag{17}$$

$$\text{CoM-}Z=\frac{\sum_{i=1}^{n}V_i(1-\alpha_{\text{g},i})Z_i}{\sum_{i=1}^{n}V_i(1-\alpha_{\text{g},i})} \tag{18}$$

where n is the total number of mesh cells, V_i represents the volume of the ith mesh cell, $\alpha_{\text{g},i}$ is the gas volume fraction in the ith mesh cell, and X_i, Y_i and Z_i denote the ith mesh cell along the X, Y and Z axes, respectively.

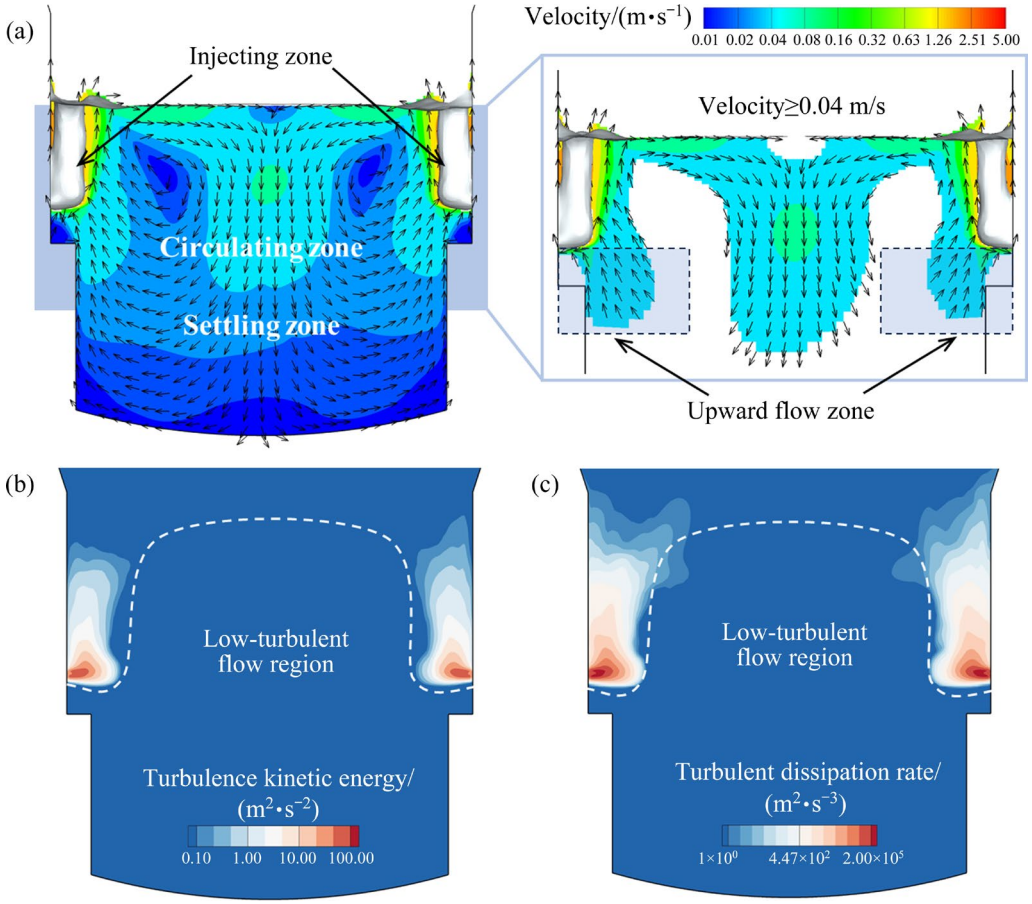

Fig. 5 Time-averaged flow field of double-side-blown gas−liquid flow (v=37 m/s, H=200 mm): (a) Time-averaged velocity distribution of liquid; (b) Time-averaged turbulence kinetic energy; (c) Time-averaged turbulence dissipation rate

The average liquid velocity ($\overline{v}$) and relative standard deviation (RSD) of the liquid velocity distribution are commonly used to quantitatively characterize the mixing intensity and uniformity of gas−liquid stirring in the numerical simulation of the copper smelting furnaces [39], calculated respectively by the following equations:

$$\overline{v}=\frac{\sum_{i=1}^{n}v_iV_i(1-\alpha_{g,i})}{\sum_{i=1}^{n}V_i(1-\alpha_{g,i})} \tag{19}$$

$$\mathrm{SD}=\sqrt{\frac{n}{n-1}\frac{\sum_{i=1}^{n}(v_i-\overline{v})V_i(1-\alpha_{g,i})}{\sum_{i=1}^{n}V_i(1-\alpha_{g,i})}} \tag{20}$$

$$\mathrm{RSD}=\frac{\mathrm{SD}}{\overline{v}}\times100\% \tag{21}$$

where v_i is the velocity in the ith mesh, and SD is the standard deviation of the liquid velocity.

The penetration depth is critical as an indicator of the gas−liquid interaction and the effectiveness of gas distribution within the liquid. To accurately monitor the PD of side-blown injected gas, the concept of equivalent penetration depth was proposed in this work. As illustrated in Fig. 6(a), the brown sampling region extends 0.04 m from the inlet area (0.0283 m < Y < 0.0316 m, 0.1219 m < Z < 0.1253 m) toward the centerline. The PD (L) was calculated according to

$$L=\frac{\sum_{i=1}^{n}\alpha_{g,i}V_i}{A_{in}} \tag{22}$$

where $\alpha_{g,i}$ represents the gas volume fraction of the ith mesh cell, and A_{in} denotes the inlet area. This algorithm ensured a continuous variation of the PD without abrupt changes and is consistent with the time-averaged field.

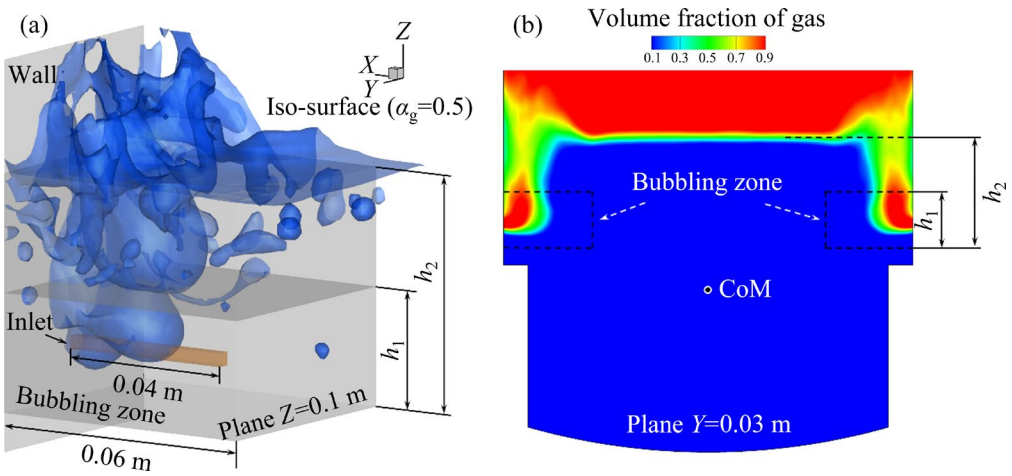

Fig. 6 Extraction range of characteristic parameters: (a) Transient flow field; (b) Time-averaged flow field

The gas hold-up rate (GHR) quantifies the fraction of the total volume occupied by the gas phase. It is important for assessing the gas−liquid interaction, the efficiency of gas dispersion, and the overall performance of the reactor.

The volume of bubbles (VoB) was determined by the total gas volume within the bubbling zone shown in Fig. 6(a), where h_1 is determined by the time-averaged gas−liquid distribution shown in Fig. 6(b). The VoB is important for evaluating gas dispersion and bubble dynamics. The total volume of the gas phase (VoG) is calculated from the gas volume within the extended region heights from h_1 to h_2, the latter being determined by the initial liquid level. The volume of the upward flow zone (VoUF) defined in this work is calculated from the total volume of liquid with velocities greater than or equal to 0.04 m/s below the plane at $Z < 0.12$ m and within 0.06 m horizontally from the nozzle.

4.1.3 Spearman correlation analysis

Correlation analysis is generally used to assess the strength or direction of correlation between mathematical and statistical variables [40]. A strong positive correlation indicates a robust relationship between variables, whereas a low correlation suggests a weak relationship. The commonly used methods for correlation analysis include Pearson correlation analysis, Spearman correlation analysis, and the Kendall rank correlation coefficient [41].

For time-series data, it is crucial to conduct a stationarity test initially to determine whether the time series are random, as random data lack analytical value. The augmented Dickey-Fuller (ADF) test [42] was applied for the stationarity testing of variables in this work, and the results are presented in Table 4. The results indicate that all parameters except the GHR are stationary data.

Table 4 Results of ADF test

Parameter	Test statistics	Critical value (1%)	*P*-value	Result
CoM-*X*	−8.68	−3.43	4.26×10^{-14}	Stationarity
CoM-*Y*	−20.4	−3.43	0.00	Stationarity
CoM-*Z*	−10.7	−3.43	3.08×10^{-19}	Stationarity
PD	−32.8	−3.43	0.00	Stationarity
VoB	−30.6	−3.43	0.00	Stationarity
VoG	−13.3	−3.43	7.24×10^{-25}	Stationarity
VoUF	−21.9	−3.43	0.00	Stationarity
GHR	−0.655	−3.43	0.858	Non-stationarity
$\overline{v}$	−12.9	−3.43	3.95×10^{-24}	Stationarity
RSD	−21.3	−3.43	0.00	Stationarity

The kernel density distribution of the standardized data is illustrated in Fig. 7(a). It is seen that all variables approximate a normal distribution. Therefore, the Spearman correlation coefficient was utilized to measure monotonic relationships between pairwise variables [43]. The Spearman correlation analysis evaluates similarity scores based on ranks, serving as a non-parametric measure of correlation that quantifies the extent of monotonic relationships, even in the absence of a linear relationship [41,44]. For two time-series data sets of equal length $A=[A_1, A_2, \cdots, A_n]$ and $B=[B_1, B_2, \cdots, B_n]$, Spearman's correlation coefficient (r_s) is defined as follows:

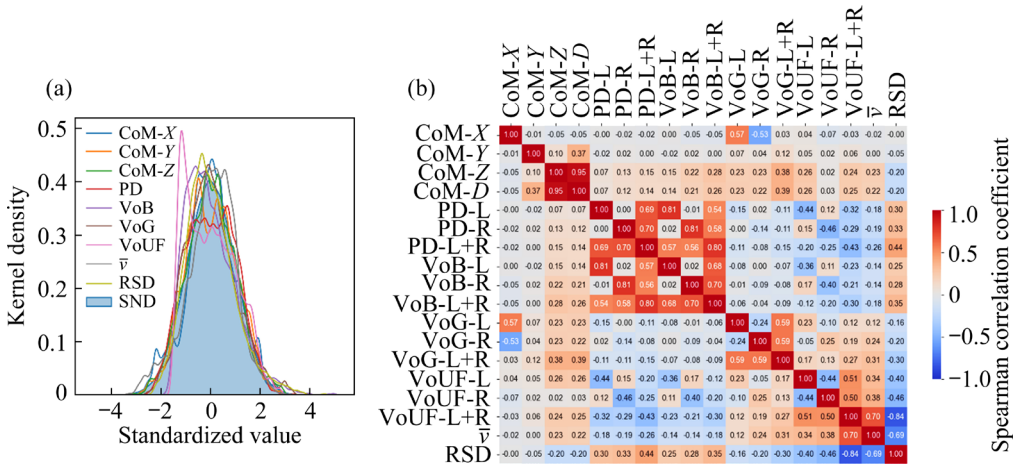

Fig. 7 Distribution of parameters and Spearman correlation coefficients: (a) Kernel density distribution of standardized data (SND: standard normal distribution); (b) Heatmap of Spearman correlation coefficients

$$r_s=\frac{\sum_{i=1}^{n}(A_i-\overline{A})(B_i-\overline{B})}{\sqrt{\sum_{i=1}^{n}(A_i-\overline{A})^2\sum_{i=1}^{n}(B_i-\overline{B})^2}} \tag{23}$$

where

$$\overline{A}=\frac{\sum_{i=1}^{n}A_i}{n},\ \overline{B}=\frac{\sum_{i=1}^{n}B_i}{n}.$$

The value of r_s ranges from −1 to 1, where 0 indicates no correlation, 1 indicates a perfect positive correlation, and −1 indicates a perfect negative correlation. The sign of r_s indicates the direction of the correlation.

The values of r_s between pairwise stationary data sets mentioned above are depicted in Fig. 7(b). Letters preceding the hyphen denote different parameters. Following the hyphen, $-X$, $-Y$, and $-Z$ correspond to the component of CoM in the X, Y, and Z directions respectively. $-D$ represents the distance of CoM in the transient field to the time-averaged field. −L denotes parameters in the left injecting area (where $X<0$), −R denotes parameters in the right injecting area (where $X>0$), and −L+R indicates the sum of parameters in the left and right injecting areas. The r_s value between PD and VoB exceeds 0.80, indicating a strong relationship between the penetration depth and the bubble volume. It is evident that an increase in the penetration depth directly increases the bubble volume. The value of r_s between PD and VoG is approximately 0, suggesting a negligible correlation between penetration depth and gas content in the injecting zone. The value of r_s between VoUF-L+R and $\overline{v}$ is 0.70, while with RSD it reaches −0.84. There is a strong positive correlation between the volume of the upward flow zone and $\overline{v}$, and a very strong negative correlation with RSD. This result indicates that changes in the volume of upward flow zones are strongly associated with the intensity and uniformity of the circulation. Additionally, the value of r_s between VoUF-L and VoUF-R is −0.48, indicating a moderate negative correlation, which suggests that there are possible alternating strengths between the circulating flows on the left and right sides. The value of r_s between CoM-X and CoM-D is 0.75, which indicates a strong relationship. The CoM of the liquid phase may be primarily caused by changes along the X-direction.

4.2 Flow patterns

4.2.1 Circulating flow

The flow patterns of the double-side-blown process are crucial for gas−liquid mixing, slag−metal separation, and stirring intensity. To further investigate the mutual influences between the two injection zones under different operating conditions, we conducted a statistical analysis of flow characteristics at various liquid levels and inlet velocities. According to Fig. 8(a), the height of the circulation center increases with increasing liquid level. This phenomenon may be attributed to the elongation of the bubble rise trajectory due to the increased liquid level, which enhances the

dissipation of the kinetic energy of injected gas. Figure 8(b) indicates that with increasing inlet velocity, the low-speed region of the circulation noticeably decreases.

As depicted in Fig. 9(a), the VoUF exhibits a trend of initially increasing and then decreasing with increasing liquid level. At H=200 mm or H=220 mm, the range of peak values of VoUF is significantly larger than that under other conditions, with the r_s values of −0.46 and −0.52 for VoUF between the left and right sides. The large VoUF indicates that the driving effect of the injected gas on the liquid phase is significantly enhanced, promoting liquid movement and thereby increasing the gas−liquid mixing and stirring efficiency. According to Fig. 10(c), the smoothed VoUF-L and VoUF-R exhibit distinct opposite trends of variation under specific conditions, whereas they demonstrate more random and disorderly variations at other liquid levels. This indicates that under certain conditions, the formation and magnitude of circulation areas on the two sides exhibit periodic alternations. Further analysis of Fig. 10(e) indicates that over short time scales, alternating dominance between VoUF-L and VoUF-R implies an imbalance in the evolution of circulation intensities over time. As shown in Fig. 9(b), with an increase in the inlet velocity, the value of r_s gradually increases, showing a linear relationship. This may be due to the enhanced circulation intensities as the inlet velocity increases, thereby gradually reducing their mutual influence.

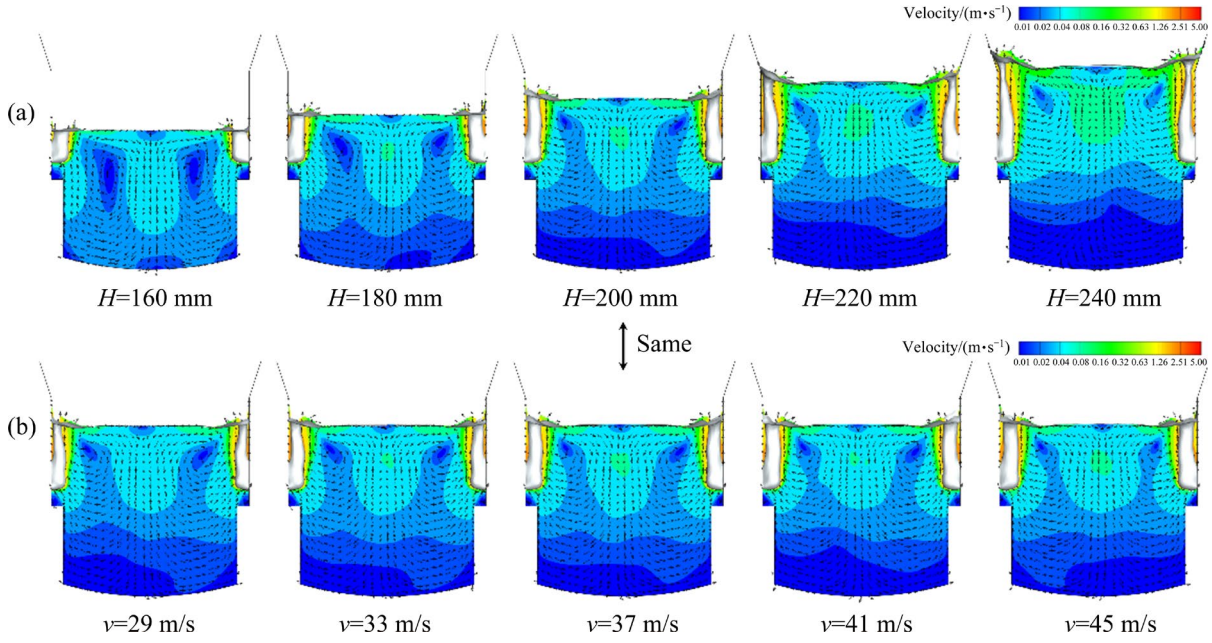

Fig. 8 Time-averaged velocity distribution and statistical analysis of VoUF: (a) Time-averaged velocity contour at different liquid levels (v=37 m/s); (b) Time-averaged velocity contour at different inlet velocities (H=200 mm)

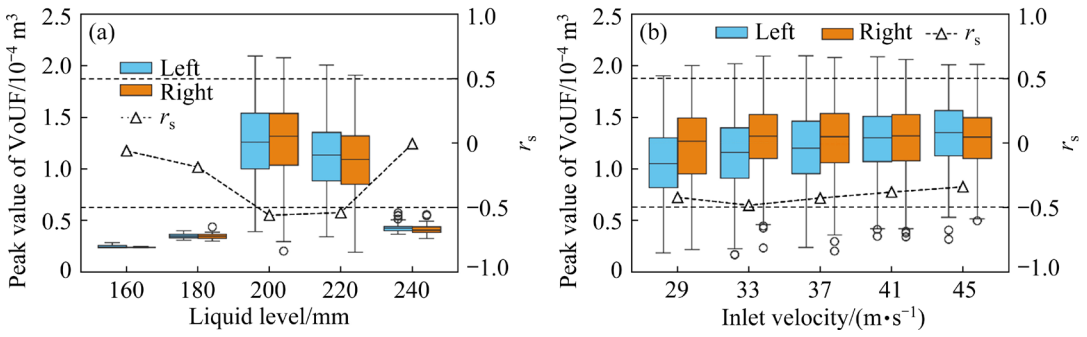

Fig. 9 Distribution of peaks of VoUF and Spearman correlation coefficients between VoUFs of two sides: (a) At different liquid levels (v=37 m/s); (b) At different inlet velocities (H=200 mm)

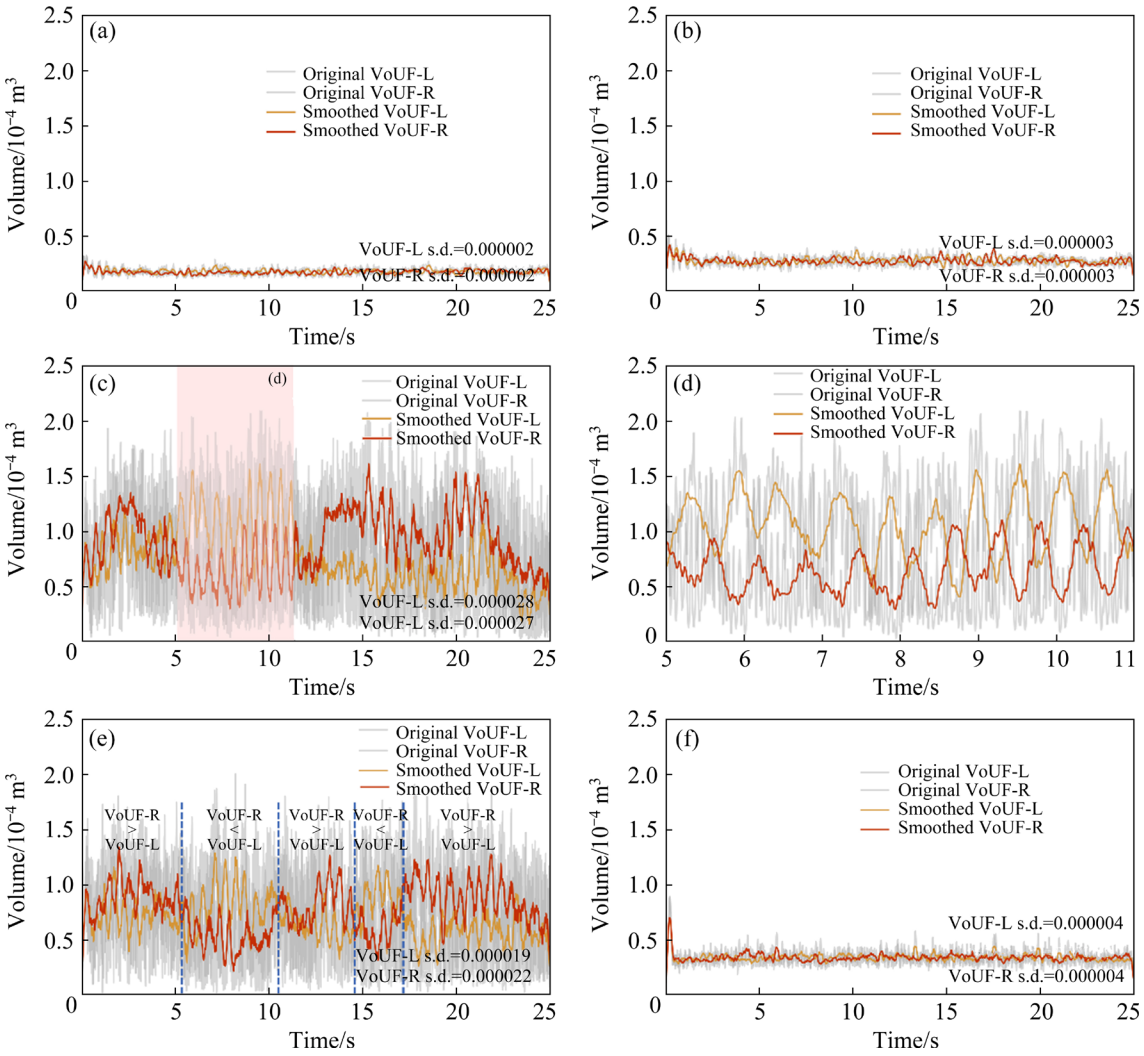

Fig. 10 VoUF over time at various liquid levels: (a) H=160 mm; (b) H=180 mm; (c, d) H=200 mm; (e) H=220 mm; (f) H=240 mm

4.2.2 Penetration depth

The PD of the gas critically influences the gas−liquid contact area, gas hold-up, and circulating flow field. To present the impact of alternating strengths of the circulating flows on bubble behavior, the dimensionless PD obtained from statistical analysis is presented in Fig. 11. The PD exhibits a parabolic relationship with the inlet velocity, with a fitness exceeding 0.99, in line with the results of WANG et al [22]. At lower velocities (v<29 m/s, corresponding to Fr < 20.6), the dimensionless PD is close to that of the single-side-blown process. The inlet velocities of the injected gas are too small to stir the liquid phase, resulting in little mutual influence between the weak circulations. At higher velocities (v > 57 m/s, corresponding to Fr > 107), the high-speed injected gas transfers more kinetic energy to the flow field, leading to the formation of strong and stable circulation regions. The bubbles formed on both sides experience resistance from the fast flows,

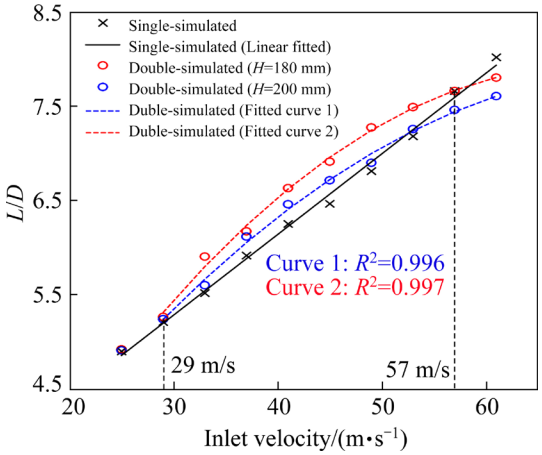

Fig. 11 Dimensionless PD at various inlet velocities

causing the PD to be even smaller than that in the single-side-blown process. Within the intermediate velocity range (29 m/s $< v <$ 57 m/s), the PD generally exceeds that of the single-side-blown process. The alternating strengths of circulation reduce the resistance of the growing bubbles from the liquid phase. Based on the characteristics of the PD, the double-side-blown gas−liquid flow can be classified into three modes: weak circulation ($v <$ 29 m/s), alternating strong−weak circulation (29 m/s $< v <$ 57 m/s), and strong circulation ($v >$ 57 m/s). At liquid levels of 180 and 200 mm, respectively, the PD in the strong-weak alternating circulation mode averages 4.2% and 2.0% greater than that in the single-side-blown process.

4.3 Liquid oscillation

4.3.1 Oscillating frequency

The liquid oscillation in the molten bath significantly affects the slag splashing, lining erosion and operational stability in the OSBF. Due to the periodic alternation of the circulating flows on both sides under the symmetric geometry and boundary conditions, it is important to analyze the variations of the CoM of the liquid phase, which reflects the overall motion of the liquid. It is shown in Figs. 12(a) and (b) that the distribution of CoM lacks apparent regularity in the three-dimensional space. Figure 12(a) indicates that increasing the liquid level significantly enlarges the range and disorder of oscillations in all three directions, especially along the X axis, consistent with the results of the correlation analysis above. Figure 12(b) suggests that at H=200 mm, the fluctuation range of the CoM in the X axis decreases as the inlet velocity increases.

The component of CoM in the X direction (CoM-X) over time and its autocorrelation analysis are presented in Figs. 13(a) and (b). The CoM-X exhibits significant periodic variations along the X axis. The frequency domain analysis using the fast Fourier transform, shown in Fig. 13(c), indicates an oscillating period of approximately 0.57 s (1/1.75 s). Furthermore, it is observed from Fig. 13(d) that with increasing liquid levels, the oscillating period of the CoM-X initially decreases and then increases. Figure 13(e) illustrates that there is no apparent correlation between the oscillating period of the CoM-X and the inlet velocity.

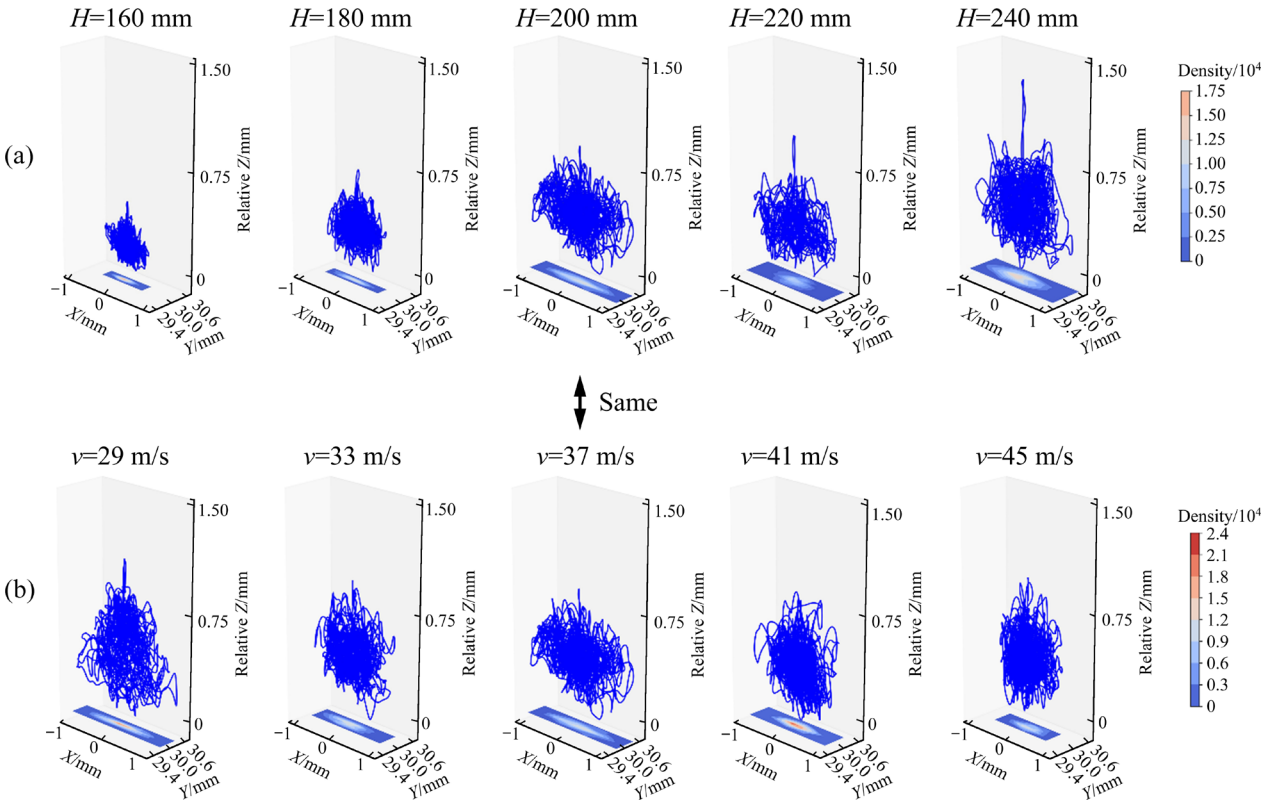

Fig. 12 Position of CoM in plane X−Y over time at different liquid levels (v=37 m/s) (a) and at different inlet velocities (H=200 mm) (b) (The contour represents the density distribution of the CoM projected onto the X−Y plane)

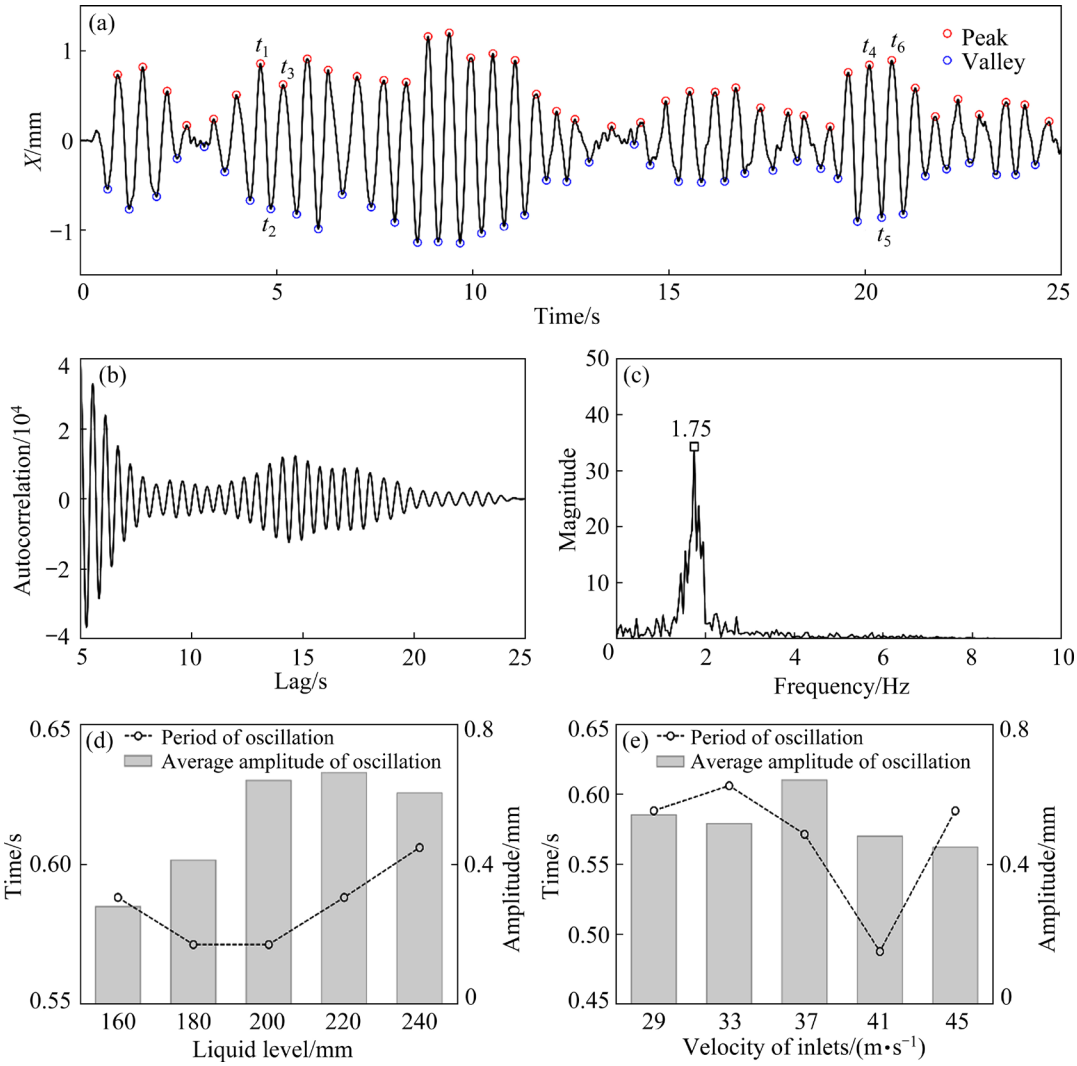

Fig. 13 Periodic oscillations of CoM-*X*: (a) Fluctuation of CoM-*X*; (b) Frequency domain analysis; (c) Autocorrelation plot; (d, e) Period and average amplitude of CoM-*X* at different liquid levels and at different inlet velocities, respectively

4.3.2 Lag correlation analysis

To investigate the primary causes for the variations of the CoM-*X*, which is the main component of liquid oscillations, we defined a ratio of the liquid phase masses on the two sides of the vessel, denoted as R_m. The formula of R_m is given as follows:

$$R_m=\frac{\Delta m}{\Delta m_0} \tag{24}$$

where Δm_0 denotes the difference in liquid phase mass between the two sides of the longitudinal section at X=0 in Fig. 14(a), and Δm represents the difference in liquid phase mass between the two sides of the longitudinal section at X=0 below the cross-section at Z=Z_0 in Fig. 14(a). A larger Δm corresponded to a larger R_m, indicating a greater contribution to the variation of liquid phase relative to CoM-*X* at the corresponding position. Figure 14(b) illustrates the variations of R_m at time t_1−t_6 within the bubble region (Z < 0.19 m), fluctuation region (0.19 m < Z < 0.22 m), and splashing region (Z > 0.22 m) corresponding to Fig. 13(a). Compared with the bubble and splashing regions, the fluctuation region exhibits the greatest variation in R_m, even exceeding 2 at t=t_2, underscoring its significant contribution to the variation of the CoM-*X*. Combined with Fig. 14(c), it is evident that the wave-like fluctuations of the liquid surface also exhibit apparent periodicity. The periodic and stable oscillations of the liquid in the *X* direction suggest that the mass transfer and circulation of the liquid phase on both sides are relatively stable in the double-side-blown process.

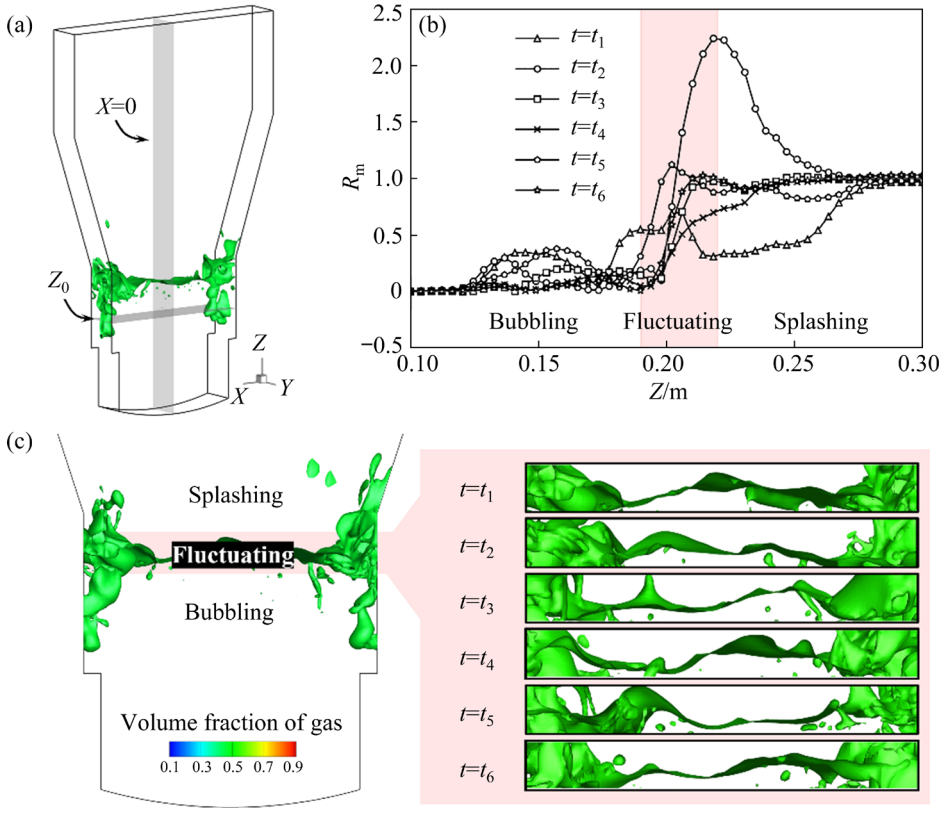

Fig. 14 Analysis of causes inducing variations of CoM-*X*: (a) Plane location; (b) R_m along *Z*-axis; (c) Fluctuation of liquid level

It is observed from Figs. 15(a) and (b) that the variations of the VoUF-L-R (the difference in the VoUF between two sides) and the CoM-*X* follow a similar trend. According to the result of lag correlation analysis shown in Fig. 15(c), non-zero peak correlation coefficients with an average interval of 0.57 s (consistent with the oscillating period of CoM-*X*) indicate a lagged relationship between VoUF-L-R and CoM-*X*. In the circulating flows of the double-side-blown process, the difference of the circulating intensities causes the liquid to predominantly flow towards the side with strong circulation, resulting in fluctuations of the liquid phase. Due to the stability of circulation on both sides and mass transfer in the central liquid phase, CoM-*X* exhibits stable periodic fluctuations along the *X* axis.

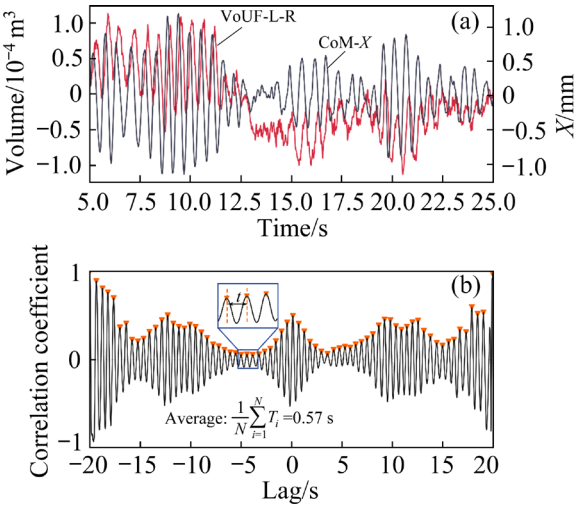

Fig. 15 Lag correlation analysis between VoUF-L-R and CoM-*X*: (a) VoUF-L-R and CoM-*X* over time at *H*=180 mm; (b) Lag correlation analysis (*H*=180 mm)

5 Conclusions

(1) The periodic bubble behavior serves as the primary driver of liquid motion and circulation, creating an upward flow zone that exhibits high sensitivity to bubble behavior with velocities exceeding 0.04 m/s. There is an alternating pattern in the volume of upward flow zone on both sides, indicating alternating strengths in the two circulating flows at certain liquid levels. This phenomenon increases the intensity of the circulating flow, which significantly enhances the efficiency of gas−liquid

stirring.

(2) Based on the effect of circulating flows on the penetration depth, the double-side-blown gas−liquid flow is categorized into three flow patterns: weak circulation, strong−weak alternating circulation, and strong circulation. In the strong−weak alternating circulation mode, the penetration depth is generally greater, indicating a stronger transfer of the kinetic energy, than that in the single-side-blown process. At a liquid level of 180 mm and an inlet velocity of 37 m/s, the penetration depth in the strong−weak alternating circulation mode averages 2.0% greater than that in the single-side-blown process.

(3) The liquid phase exhibits relatively stable and periodic oscillations in the horizontal injection direction due to the imbalance of circulating intensities on both sides. With increasing liquid levels, the oscillating period in the injecting direction initially decreases and then increases.

CRediT authorship contribution statement

Wei WANG: Conceptualization, Methodology, Software, Data curation, Writing − Original draft; **Hongliang ZHAO:** Conceptualization, Project administration, Supervision, Funding acquisition, Writing − Review & editing; **Feng-qin LIU:** Conceptualization, Project administration, Supervision, Funding acquisition; **Hong Yong SOHN:** Conceptualization, Writing − Review & editing.

Declaration of competing interest

The authors declare that they have no known competing financial interests or personal relationships that could have appeared to influence the work reported in this paper.

Acknowledgments

The authors would like to acknowledge the financial support for this research work from the National Key Research and Development Program of China (No. 2022YFB3304901).

References

[1] CHEN Lin, CHEN Wei, XIAO Hui, YANG Tian-zu, LIU Wei-feng, ZHANG Du-chao. Oxygen-rich side blow bath smelting technology: New developments in China [C]//7th International Symposium on High-Temperature Metallurgical Processing. Cham: Springer International Publishing, 2016: 123−130.

[2] CHEN Peng, XIAO Hui, CHEN Jiang, CHEN Lin, ZHANG Du-chao, LIU Wei-feng, YANG Tian-zu. Oxygen-rich side-blown bath smelting of copper dross: A process study [J]. Journal of Sustainable Metallurgy, 2020, 6(2): 344−354.

[3] BIAN Zhi-wei, CHEN De-sheng, SUN Lin-quan, WANG Li-na, ZHAO Hong-xin, ZHEN Yu-lan, QI Tao. Numerical simulation of multiphase flow in ironmaking process for oxygen-rich side-blown bath smelting furnace [J]. Metallurgical and Materials Transactions B, 2023, 54(3): 1352−1367.

[4] ZHU Shuai, ZHAO Qiu-yue, LI Xiao-long, LIU Yan, ZHANG Ting-an. CFD simulation of gas-slag-metal multiphase flow in a side-blown vortex smelting reduction reactor [J]. Journal of Sustainable Metallurgy, 2023, 9(3): 1033−1049.

[5] CHEN Lin, YANG Tian-zu, BIN Shu, LIU Wei-feng, ZHANG Du-chao, BIN Wan-da, ZHANG Li. An efficient reactor for high-lead slag reduction process: Oxygen-rich side blow furnace [J]. JOM, 2014, 66(9): 1664−1669.

[6] ZHU Zhen-yu, ZHOU Ping, WAN Xing-bang, CHEN Zhuo, ZHANG Ling, KUANG Shi-bo. CFD modeling of gas−liquid flow phenomenon in lead smelting oxygen-enriched side-blown furnace [J]. Transactions of Nonferrous Metals Society of China, 2024, 34(8): 2671−2685.

[7] ZHU Zhen-yu, ZHOU Ping, CHEN Zhuo, LONG Peng, ZHANG Lin. Numerical simulation on effect of air injection on two-phase flow in oxygen enriched side-blown furnace [J]. Journal of Central South University (Science and Technology), 2022, 53(2): 398−408. (in Chinese)

[8] ZHOU Ao, ZHANG Le-ru, ZHOU Yu-gao, LI Yong-bin, WU Xiao-song, XIA Long-gong, LIU Zhi-hong. Co-smelting process of Pb concentrate and Zn leaching residues with oxygen-rich side blowing furnaces: Industrial application and material balance [J]. JOM, 2023, 75(12): 5833−5846.

[9] MUKHANOV B K, SULEIMENOV A, WÓJCIK W, GROMASZEK K. Development of an optimal control system for smelting process in the molten-pool [J]. Przeglad Elektrotechnichniczny, 2012, 88(11): 366−368.

[10] HE Mao-qi, YU Gang, YANG Chong, HAN Long. Dynamic soft sensor modeling of matte grade in copper oxygen-rich side blow bath smelting process [J]. Measurement, 2023, 223: 113792.

[11] SONG Ke-zhou, JOKILAAKSO A. Transport phenomena in copper bath smelting and converting processes—A review of experimental and modeling studies [J]. Mineral Processing and Extractive Metallurgy Review, 2022, 43(1): 107−121.

[12] ANDERSON A, KUMAR V, RAO V M, GROGAN J. A review of computational capabilities and requirements in high-resolution simulation of nonferrous pyrometallurgical furnaces [J]. JOM, 2022, 74(4): 1543−1567.

[13] ZHU Jun, XUE Jing-jing, TIAN Qing-zhang, ZENG Wen-bin, YUAN Chun. Research on physical modeling of nonferrous metals bath smelting [J]. Foundry Technology, 2012, 33(1): 48−51. (in Chinese)

[14] BIAN Zhi-wei, CHEN De-sheng, SUN Lin-quan, WANG Li-na, ZHAO Hong-xin, ZHEN Yu-lan, QI Tao. Numerical simulation and experimental investigation of multiphase flow in an oxygen-rich side-blown bath smelting furnace [J]. JOM, 2023, 75(9): 3962−3974.

[15] ZHU Shuai, ZHAO Qiu-yue, LI Xiao-long, LIU Yan, LI Tian-ci, ZHANG Ting-an. Flow and penetration behavior of submerged side-blown gas [J]. International Journal of

Minerals, Metallurgy and Materials, 2023, 30(6): 1067−1077.
[16] KAPUSTA J P T. Submerged gas jet penetration: A study of bubbling versus jetting and side versus bottom blowing in copper bath smelting [J]. JOM, 2017, 69(6): 970−979.
[17] LIU Fan-han. Characteristics analysis of the side-blown gas jet mixing process [J]. Proceedings of the Institution of Mechanical Engineers, Part C: Journal of Mechanical Engineering Science, 2021, 235(20): 4838−4850.
[18] JIANG Xu, CUI Zhi-xiang, CHEN Mao, ZHAO Bao-jun. Mixing behaviors in the horizontal bath smelting furnaces [J]. Metallurgical and Materials Transactions B, 2019, 50(1): 173−180.
[19] LI Xiao-long, LIU Yan, WANG Dong-xing, ZHANG Ting-an. Emulsification and flow characteristics in copper oxygen-rich side-blown bath smelting process [J]. Metals, 2020, 10(11): 1520.
[20] HOEFELE E O, BRIMACOMBE J K. Flow regimes in submerged gas injection [J]. Metallurgical Transactions B, 1979, 10(4): 631−648.
[21] MA Ji, ZHOU Ping, CHENG Wei, SONG Yan-po, SHI Peng-yu. Dimensional analysis and experimental study of gas penetration depth model for submerged side-blown equipment [J]. Experimental Thermal and Fluid Science, 2016, 75: 220−227.
[22] WANG shu-xiao, CHEN Xue-gang, WEN Zhi. Experimental study on gas flow penetration and stirring behavior in side-blowing furnace [J]. China Nonferrous Metallurgy, 2021, 50(6): 97−102. (in Chinese)
[23] LIU Yan-ting, YANG Tian-zu, CHEN Zhuo, ZHU Zhen-yu, ZHANG Ling, HUANG Qing. Experiment and numerical simulation of two-phase flow in oxygen enriched side-blown furnace [J]. Transactions of Nonferrous Metals Society of China, 2020, 30(1): 249−258.
[24] MA Ji, SONG Yan-po, ZHOU Ping, CHENG Wei, CHU Shi-gan. A mathematical approach to submerged horizontal buoyant jet trajectory and a criterion for jet flow patterns [J]. Experimental Thermal and Fluid Science, 2018, 92: 409−419.
[25] XIAO Ya-dong, WANG Jie, LU Ting-ting, LIU Feng-qin, LV Chao, ZHAO Hong-liang. An experimental study on gas–liquid flow and mixing behavior in a copper side-blown smelting furnace [J]. Metallurgical and Materials Transactions B, 2023, 54(2): 756−764.
[26] XIAO Ya-dong, LU Ting-ting, ZHOU Yu-gao, SU Qiu-qiong, MU Liang-zhao, WEI Tao, ZHAO Hong-liang, LIU Feng-qin. Computational fluid dynamics study on enhanced circulation flow in a side-blown copper smelting furnace [J]. JOM, 2021, 73(9): 2724−2732.
[27] HU Jun-yi, YANG Shi-liang, WANG Hua. VOF study of mesoscale bubble flow dynamics in the side-blown gas–liquid two-phase reactor [J]. Chemical Engineering Journal, 2024, 480: 147983.
[28] WAN Zhang-hao, YANG Shi-liang, WANG Hua. Multiphase stirring dynamics of gas-slag-matte in large-scale side-blown copper bath smelting process [J]. Journal of Sustainable Metallurgy, 2024, 10(2): 992−1006.
[29] BIAN Zhi-wei, CHEN De-sheng, SUN Lin-quan, WANG Li-na, ZHAO Hong-xin, ZHEN Yu-lan, QI Tao. Numerical simulation and optimization analysis of primary air injection mode in oxygen-rich side-blown bath smelting furnace [J]. Journal of Sustainable Metallurgy, 2023, 9(2): 871−883.
[30] SU Xin-tao, WANG Shi-bo, WANG Hua, XU Jian-xin, XIAO Qing-tai. Numerical simulation study of the effect of nonlinear side blowing on the flow of gas-liquid two-phase flow [J]. International Journal of Chemical Reactor Engineering, 2024, 22(4): 365−382.
[31] ZHOU Ping, CHENG Wei, MA Ji, XIA Zhong-wei, LIAO Zhou. Experimental study on side-blown flowing characteristics [J]. Journal of Central South University (Science and Technology), 2016, 47(8): 2879−2883. (in Chinese)
[32] WANG Shu-xiao, WEN Zhi, XING Yi, CHEN Xue-gang, LIU Xun-liang. Hydraulic experiment on macro-instability in the lead smelting side-blown furnace [J]. Journal of Physics: Conference Series, 2024, 2738(1): 012008.
[33] SHUI Lang, CUI Zhi-xiang, MA Xiao-dong, RHAMDHANI M A, NGUYEN A V, ZHAO Bao-jun. Understanding of bath surface wave in bottom blown copper smelting furnace [J]. Metallurgical and Materials Transactions B, 2016, 47(1): 135−144.
[34] SHUI Lang, MA Xiao-dong, CUI Zhi-xiang, ZHAO Bao-jun. An investigation of the behavior of the surficial longitudinal wave in a bottom-blown copper smelting furnace [J]. JOM, 2018, 70(10): 2119−2127.
[35] OBISO D, REUTER M, RICHTER A. CFD investigation of rotational sloshing waves in a top-submerged-lance metal bath [J]. Metallurgical and Materials Transactions B, 2021, 52(4): 2386−2394.
[36] TERNSTEDT P, NI P Y, LUNDQVIST N, TILLIANDER A, JÖNSSON P G. A physical modelling study to determine the influence of slag on the fluid flow in the AOD converter process [J]. Ironmaking & Steelmaking, 2018, 45(10): 944−950.
[37] FABRITIUS T M J, MURE P T, HÄRKKI J J. The determination of the minimum and operational gas flow rates for sidewall blowing in the AOD-converter [J]. ISIJ International, 2003, 43(8): 1177−1184.
[38] KULKARNI A A, JOSHI J B. Bubble formation and bubble rise velocity in gas−liquid systems: A review [J]. Industrial & Engineering Chemistry Research, 2005, 44(16): 5873−5931.
[39] LU Ting-ting, MU Liang-zhao, XIAO Ya-dong, ZHAO Hong-liang, LIU Feng-qin. CFD study on bottom-blown copper smelting furnace with unsymmetric gas injection [J]. Journal of Sustainable Metallurgy, 2022, 8(3): 1235−1244.
[40] AKOGLU H. User's guide to correlation coefficients [J]. Turkish Journal of Emergency Medicine, 2018, 18(3): 91−93.
[41] HAUKE J, KOSSOWSKI T. Comparison of values of Pearson's and Spearman's correlation coefficients on the same sets of data [J]. Quaestiones Geographicae, 2011, 30(2): 87−93.
[42] DICKEY D A, FULLER W A. Distribution of the estimators for autoregressive time series with a unit root [J]. Journal of the American Statistical Association, 1979, 74(366a): 427−431.
[43] SCHOBER P, BOER C, SCHWARTE L A. Correlation coefficients: Appropriate use and interpretation [J]. Anesthesia & Analgesia, 2018, 126(5): 1763−1768.
[44] REBEKIĆ A, LONČARIĆ Z, PETROVIĆ S, MARIĆ S. Pearson's or Spearman's correlation coefficient-which one to use? [J]. Poljoprivreda, 2015, 21(2): 47−54.

基于 CFD 计算的双侧吹气液流动特性

王 维[1,2]，赵洪亮[1,2]，刘风琴[1,2]，Hong Yong SOHN[3]

1. 北京科技大学 绿色低碳钢铁冶金全国重点实验室，北京 100083；
2. 北京科技大学 冶金与生态工程学院，北京 100083
3. Department of Materials Science and Engineering, The University of Utah, Salt Lake City, Utah 84112, USA

摘 要：采用基于 CFD 数值模型定量分析了双侧吹气液流的流动特性。通过提取关键参数，并使用 Spearman 相关性分析量化气泡行为、循环流动和液相晃动之间的关系。结果表明，稳定喷吹下的周期性气泡行为驱动液体两侧的循环流动。两侧气泡行为的不对称导致循环流动强度的交替变化，显著提高 200 和 220 mm 特定液位下的气液混合效率。基于循环流动对穿透深度的影响，双侧吹气过程的流动模式被分为弱循环、强弱交替循环和强循环模式。在强弱交替循环模式下，穿透深度通常大于单侧吹气过程。两侧循环强度的不平衡导致液面在喷吹方向形成稳定的波动，这揭示熔池中出现周期性晃动。此外，还研究了液位和气体流速等参数对液相晃动的影响。

关键词：数值模拟；侧吹炉；流动特征；气泡行为；穿透深度；Spearman 相关性分析

(Edited by Xiang-qun LI)